PHYSICAL REVIEW B **100**, 064429 (2019)

Editors' Suggestion

Topological Hall effect and emergent skyrmion crystal at manganite-iridate oxide interfaces

Narayan Mohanta,[1] Elbio Dagotto,[1,2] and Satoshi Okamoto[1]
[1]*Materials Science and Technology Division, Oak Ridge National Laboratory, Oak Ridge, Tennessee 37831, USA*
[2]*Department of Physics and Astronomy, The University of Tennessee, Knoxville, Tennessee 37996, USA*

(Received 23 May 2019; revised manuscript received 13 July 2019; published 30 August 2019)

Scalar spin chirality is expected to induce a finite contribution to the Hall response at low temperatures. We study this spin-chirality-driven Hall effect, known as the topological Hall effect, at the manganite side of the interface between $La_{1-x}Sr_xMnO_3$ and $SrIrO_3$. The ferromagnetic double-exchange hopping at the manganite layer, in conjunction with the Dzyaloshinskii-Moriya (DM) interaction which arises at the interface due to broken inversion symmetry and strong spin-orbit coupling from the iridate layer, could produce a skyrmion-crystal (SkX) phase in the presence of an external magnetic field. Using the Monte Carlo technique and a two-orbital spin-fermion model for manganites, supplemented by an in-plane DM interaction, we obtain phase diagrams which reveal at low temperatures a clear SkX phase and also a low-field spin-spiral phase. Increasing temperature, a skyrmion-gas phase, precursor of the SkX phase upon cooling, was identified. The topological Hall effect primarily appears in the SkX phase, as observed before in oxide heterostructures. We conclude that the manganite-iridate superlattices provide another useful platform to explore a plethora of unconventional magnetic and transport properties.

DOI: 10.1103/PhysRevB.100.064429

I. INTRODUCTION

The interplay between spin-orbit coupling and magnetism has led to the emergence of several novel properties at the interface between distinct transition-metal oxides, such as the anomalous Hall effect [1–3] and the anisotropic magnetoresistance [4]. Another source of the Hall effect in a heterointerface with both time-reversal and mirror symmetries broken is provided by real-space noncollinear magnetic textures with a finite scalar spin chirality $\mathbf{S}_i \cdot (\mathbf{S}_j \times \mathbf{S}_k)$ [5–8]. This spin chirality generates an effective electromagnetic field for electrons through the spin Berry phase mechanism. The resulting Hall effect, known as the topological Hall (TH) effect, has been observed in perovskite oxides [9–12], chiral magnets [13,14], frustrated magnets [15], and Heusler alloys [16–18].

In compounds with heavy elements and without inversion symmetry, the antisymmetric spin exchange such as the Dzyaloshinskii-Moriya (DM) interaction $\mathbf{D}_{ij} \cdot (\mathbf{S}_i \times \mathbf{S}_j)$, coexisting with a ferromagnetic (FM) exchange $\mathbf{S}_i \cdot \mathbf{S}_j$, favors a spin-spiral (SS) phase (characterized by a single wave number $\mathbf{q}$) [19,20]. In the presence of an external magnetic field or an easy-plane anisotropy, the SS competes with ferromagnetism, and a skyrmion-crystal (SkX) phase (with three characteristic $\mathbf{q}$ values) emerges at intermediate field strengths [21–24]. The critical magnetic fields were obtained analytically and numerically in Ref. [25]. Another possible route to the SkX phase, with higher topological quantum numbers, is to realize a Kondo-type exchange coupling between itinerant electrons and localized spins, instead of the DM interaction [26,27].

An interface between the ferromagnetic metal $La_{1-x}Sr_xMnO_3$ (LSMO) with active $3d$ orbitals and the paramagnetic semimetal $SrIrO_3$ (SIO) with active $5d$ orbitals, is expected to possess a strong DM interaction arising from the spin-orbit coupling in SIO and broken structural inversion symmetry at the interface. The DM interaction, in bilayers of SIO and $SrRuO_3$, also has been found to appear primarily near the interface [9]. The presence of an interface DM interaction is supported by the small lattice mismatch at the interface (lattice constants of SIO and LSMO are 0.394 nm [28] and 0.388 nm [29], respectively) and a strain-dependent charge transfer [30]. Because of two approximate in-plane mirror symmetries, one mirror plane involves two Mn sites and another reflects two Mn sites, it is reasonable to expect that this DM vector lies in the plane of the interface [31,32]. Having an in-plane DM vector excludes the possibility of stabilizing a conical phase which typically appears in cubic systems such as MnSi [33,34]. On the other hand, LSMO, which is well known to contain several fascinating magnetic phases varying the electronic concentration [35–38], here is considered to be optimally doped with regards to the FM phase. The LSMO-SIO interface is, therefore, a promising platform to search for exotic magnetic textures such as the SkX phase.

In this paper, we theoretically investigate the formation of the SkX crystal phase at the LSMO-SIO interface and the influence of the noncollinear spin textures on the transverse Hall conductance. We use a spin-fermion model, where itinerant electrons and localized spins are coupled via a Hund interaction, and employ a numerically exact Monte Carlo (MC) method [35]. To handle large systems, we employ the traveling-cluster approach [39,40] that allows us to explore the finite-temperature behavior of the SS and the SkX phases. Indeed, one of the main results of the present study is that we observed a SkX phase with Néel-type skyrmions within a range of magnetic fields at low temperatures. Thermal fluctuations give rise to a related phase with spatially disordered nucleated skyrmions, a skyrmion gas (SkG), that prevails outside of the SkX phase at higher temperatures and acts as a precursor of the SkX phase upon cooling. Also a metastable phase with mixed bimerons and skyrmions (BM + Sk) [41] appears at finite temperatures between the SS and SkX phases. We construct phase diagrams in the temperature−magnetic field plane which describe the parameter regimes where the TH effect dominantly appears. Our study employs a widely used and realistic model of itinerant fermions in LSMO, namely the two-orbital double exchange model. While many of our conclusions are qualitatively similar to those obtained with simpler models of localized spins, in our case we can provide more accurate values for couplings and critical temperatures and also calculate the Hall conductance.

The strength of the DM interaction depends crucially on several geometrical parameters, such as the thickness of the SIO layer [9]. This offers an external tunability of the interfacial DM interaction and the resulting TH effect. The phase diagrams, obtained at different strengths of the DM interaction thus serve as a guidance to the DM interaction-control of the TH effect. In addition, we also compute the $T = 0$ phase diagram by comparing the total energies of ideal SS, SkX, and FM phases and found a reasonable agreement with the low-T properties, obtained using the MC method.

The paper is organized as follows. In Sec. II, a lattice model is defined, containing the two-orbital double-exchange model to describe a manganite region, supplemented by the DM interaction and the easy-plane anisotropy. We also outline the methodology of MC annealing and computation of physical quantities. In Sec. III, we present the MC results, revealing the emergence of the SkX phase and its consequences on the transverse Hall conductance. In Sec. IV, we show the finite-temperature behavior of different phases, obtained using Monte Carlo calculations and discuss the magnetic field versus temperature phase diagrams. Section V describes the $T = 0$ phase diagram obtained from the total energy calculation using ideal spin configurations. In Sec. VI, we discuss the relevance of the present results to possible experiments on LSMO-SIO films and superlattices, and summarize our results.

II. MODEL AND METHOD

A. Spin-fermion Hamiltonian

We consider a square lattice which hosts the essential features of LSMO at the two-dimensional interface with SIO, i.e., the intrinsic magnetism of the manganite layer, supplemented by the induced DM interaction due to the spin-orbit coupling at the iridate layer. To describe the hopping of electrons, we use a two-orbital double-exchange Hamiltonian at infinite Hund's coupling. As explained, the DM interaction arises from the influence of the iridate layer. Then the resulting spin-fermionic Hamiltonian for the LSMO-SIO interface is given by

$$\begin{aligned}\mathcal{H} = &- \sum_{\langle ij\rangle,\alpha,\beta} \left(t^{w}_{\alpha\beta}\Omega_{ij}c^{\dagger}_{i\alpha}c_{j\beta} + \text{H.c.}\right) - \sum_{\langle ij\rangle} \mathbf{D}_{ij}\cdot(\mathbf{S}_i \times \mathbf{S}_j)\\ &- h_z\sum_i S_{zi} + A\sum_i |S_{zi}|^2 - \mu\sum_{i,\alpha} c^{\dagger}_{i\alpha}c_{i\alpha}, \qquad (1)\end{aligned}$$

where $c^{\dagger}_{i\alpha}$ ($c_{i\alpha}$) is the fermionic creation (annihilation) operator at site i with position $\mathbf{r}_i$ and orbital α, $t^{w}_{\alpha\beta}$ denotes the nearest-neighbor hopping amplitudes between orbitals α and β along the hopping direction $w = x, y$, and is given by $t^x_{aa} = t^y_{aa} = 3t^x_{bb} = 3t^y_{bb} = -\sqrt{3}t^x_{ab} = -\sqrt{3}t^x_{ba} = \sqrt{3}t^y_{ab} = \sqrt{3}t^y_{ba} = 3t_0/4$; a and b represent the Mn e_g orbitals, $d_{x^2-y^2}$ and $d_{3z^2-r^2}$, respectively [35]; the DM vector, acting between nearest-neighbor lattice sites i and j, is given by $\mathbf{D}_{ij} = D(\mathbf{r}_i - \mathbf{r}_j) \times \hat{z}/|\mathbf{r}_i - \mathbf{r}_j|$ with D being the strength of the DM interaction; h_z is the external magnetic field, applied perpendicular to the interface plane; A is the strength of the easy-plane anisotropy, originating from interfacial strain and Rashba spin-orbit coupling [31], which is not explicitly included in Eq. (1); Ω_{ij} is the effective hopping at infinite Hund's coupling [42], which in terms of the polar and azimuthal spin angles θ and ϕ (assuming the electron spin $\mathbf{S}$ to be described by a classical vector in three dimensions with amplitude $S = 3/2$) is given by $\Omega_{ij} = \cos(\theta_i/2)\cos(\theta_j/2) + e^{-i(\phi_i-\phi_j)}\sin(\theta_i/2)\sin(\theta_j/2)$; μ is the chemical potential. We use a square lattice of dimension $N_x \times N_y$ and numerically solve Hamiltonian (1) using the MC technique to study the spin configuration and transport properties at different sets of parameters. We set the hopping amplitude to $t_0 = 1$ and the anisotropy parameter to $A = 0.05$ throughout the MC analysis. Then the control parameters in the model *viz.* h_z, T, D, and A are all defined in units of t_0 and the values of these parameters in realistic units are discussed in Sec. VI.

During our simulation, we set $\mu = 0$, where the corresponding electron density is one electron per site. Previous investigations [37] showed that at this density the ground state at $D = A = h_z = 0.0$ and small electron-phonon coupling is ferromagnetic, as expected from the double-exchange mechanism, properly representing the physics of LSMO. Small deviations from this electronic density are only expected to introduce small variations in our results as long as the ground state remains ferromagnetic under the conditions expressed above. If the electronic density variations are large, then other phases [35,38] may become stable instead.

B. Monte Carlo annealing

To obtain the spin configuration at a particular set of parameters, we start at a high temperature $T = 5$ and slowly cool the system down to a desired T. In each annealing session, 1000 temperature steps were employed and at each T, 2×10^5 number of MC steps were used for the spin-configuration update according to the Metropolis algorithm. To avoid the possibility of becoming trapped in a metastable spin configuration, it is important to perform a very slow annealing. In fact, we tried a variety of temperature steps: using, for example, just 50 it is certainly not sufficient for a proper convergence. In each MC step, the spin angle θ or ϕ was changed randomly to $\theta \pm \Delta\theta$ or $\phi \pm \Delta\phi$, respectively, where $\Delta\theta$ and $\Delta\phi$ are the step sizes of the angles, set to 5 degrees throughout the paper. The diagonalization of the fermionic part of the Hamiltonian is numerically expensive and to alleviate this problem, we used the traveling-cluster update scheme [39,40], in which a smaller cluster of size $N_{xc} \times N_{yc}$ is used for the MC spin update. The results presented here were obtained using a 20×20 lattice and 5×5 traveling cluster, with open-boundary conditions. We checked, with a larger lattice of size 32×32 (see results below) and a larger traveling cluster of size 10 × 10, for any finite-size effects and obtained a consistent description. The observables were calculated from the thermalized spin configurations and were MC averaged, at each T and h_z, with 100 different realizations.

C. Calculation of observables

1. Skyrmion number

A magnetic skyrmion has a distinct topological structure and when the underlying lattice is transformed from a torus to a sphere, the skyrmion gives a full coverage of the sphere. This unique feature enables skyrmions to be classified by a topological index, called the skyrmion number, which is expressed as [43,44]

$$N_{sk} = \frac{1}{4\pi}\int \mathbf{S}\cdot\left(\frac{\partial \mathbf{S}}{\partial x}\times\frac{\partial \mathbf{S}}{\partial y}\right)dxdy. \quad (2)$$

In practice for a square lattice with discrete points, the integration in Eq. (2) was performed by using a summation over the underlying lattice sites and the partial derivatives have been calculated using a central-difference scheme within the five-point stencil method [45].

2. Spin correlation function

An important quantity to identify magnetic phases and track thermodynamic phase transitions is the spin correlation function. We take the Fourier transform of the real-space spin-spin correlation function as follows:

$$S_{\mathbf{q}} = \frac{1}{N}\sum_{ij}^{|\mathbf{r}_{ij}|<\delta}\langle \mathbf{S}_i\cdot\mathbf{S}_j\rangle e^{-i\mathbf{q}\cdot\mathbf{r}_{ij}}, \quad (3)$$

where $\mathbf{S}_i$ denotes the localized spin at site i, $\mathbf{r}_{ij}$ is the distance between sites i and j, δ is the radius of a circle around site i within which all sites are considered to calculate the correlation function, and N is the total number of lattice sites. We use the radius δ up to $N_x/2$. If some sites j landed outside the full cluster, they were discarded. The quantity in Eq. (3) can be compared to intensity measured in neutron-scattering experiments, and therefore, we use the Bragg intensity as $I(\mathbf{q}) = S_{\mathbf{q}}$.

3. Hall conductance

The transverse Hall conductance is obtained by the current-current correlation function, described by the Kubo formula [6], as given below:

$$\sigma_{xy} = \frac{e^2}{h}\frac{2\pi}{N}\sum_{\epsilon_m\neq\epsilon_n}\frac{f_m - f_n}{(\epsilon_m-\epsilon_n)^2+\eta^2}\mathrm{Im}(\langle m|\hat{j}_x|n\rangle\langle n|\hat{j}_y|m\rangle), \quad (4)$$

where f_m is the Fermi function at temperature T and energy ϵ_m, $\hat{j}_w = i\sum_{i\alpha\beta}(t^w_{\alpha\beta}\Omega_{i,i+w}c^\dagger_{i\alpha}c_{i+w\beta} - t^{w*}_{\alpha\beta}\Omega^*_{i,i+w}c^\dagger_{i+w\beta}c_{i\alpha})$ is the current operator along direction $w(=x,y)$, and η is the relaxation rate. In the following, we present results with $\eta = 0.1$ because it mimics the bulk limit better than smaller η, which develops sharp peak features in the density of state due to the finite-size effect. Typically, the Hall conductance increases (decreases) slowly with decreasing (increasing) η, but its dependence on other parameters does not change. Moreover, the same value $\eta = 0.1$ was used in a previous similar study [6].

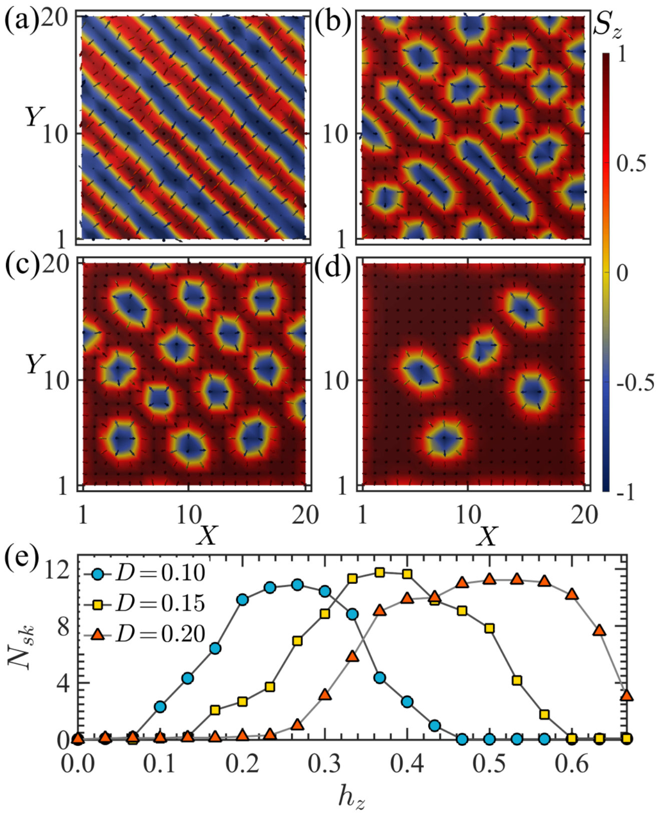

FIG. 1. Typical real-space spin configurations (a)–(d) obtained during the Monte Carlo time evolution on a 20 × 20 cluster with open boundary conditions, revealing spin-spiral (SS), mixed bimeron + skyrmion (BM + Sk), skyrmion crystal (SkX), and skyrmion gas (SkG) phases at different magnetic fields (h_z) and temperatures (T) given by (a) $h_z = 0$, $T = 0.001$, (b) $h_z = 0.2$, $T = 0.001$, (c) $h_z = 0.27$, $T = 0.001$, and (d) $h_z = 0.27$, $T = 0.15$, respectively, at a fixed value of the DM interaction $D = 0.1$. The arrows denote the in-plane components $(\mathbf{S}_{xi}, \mathbf{S}_{yi})$ while the color bar represents the normalized perpendicular component of magnetization $\mathbf{S}_{zi}$. (e) Variation of the skyrmion number N_{sk} as a function of h_z, at the values of D. The results show a clear enhancement in N_{sk} within a range of field values. The hopping amplitude is fixed to $t_0 = 1$ and the anisotropy strength to $A = 0.05$.

III. EMERGENCE OF SKYRMION CRYSTAL

We started our effort by confirming the well-known fact that the double-exchange hopping term in the absence of the DM interaction and magnetic field, yields a FM phase at low temperatures $T \lesssim 0.2$ [37]. Then, after incorporating a finite DM interaction, a single-**q** SS phase appears at low temperatures, as shown in Fig. 1(a) at $T = 0.001$. With increasing the DM strength D, the period of the spiral decreases gradually. There are two degenerate, diagonally opposite spiral solutions which often merge together to form a labyrinth-like metastable spin configuration. This type of metastable spin configuration can be avoided by re-annealing the spin configuration obtained at low T from the previous MC annealing process. To perform the re-annealing process,

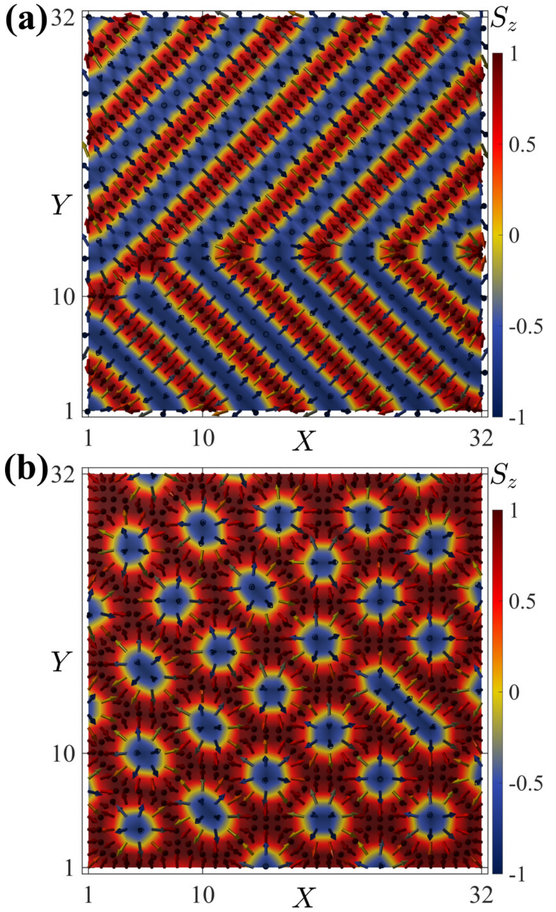

FIG. 2. Monte Carlo results using a 32×32 lattice at (a) $h_z = 0.0$ and (b) $h_z = 0.2$ showing that they are similar to those obtained with a smaller 20×20 lattice, confirming that size effects are small. These results were obtained with a DM interaction strength $D = 0.1$ and easy-plane anisotropy strength $A = 0.05$, at temperature $T = 0.001$.

we take the previous annealed spin configuration to a temperature $T = 0.5$ and slowly cool down to the lowest temperature $T = 0.001$. We considered 20 re-annealing sessions to obtain a stable spin configuration. Results using a 32×32 lattice (see Fig. 2) confirm that size effects are small.

Following this multiple-annealing process, in the presence of an external magnetic field we observed that, beyond a critical field h_z, the SS phase is transformed into a SkX phase where the skyrmions arrange themselves in a nearly triangular crystal, as depicted in Fig. 1(c) at $h_z = 0.27$ and $T = 0.001$.

Thermal fluctuations introduce a metastable regime, a mixed bimeron + skyrmion (BM + Sk) phase, between the SS and the SkX phase (similar results are obtained using vacancies [46]), as shown in Fig. 1(b) at $h_z = 0.2$ and $T = 0.001$. The bimerons are extended skyrmions and have finite contributions to the scalar spin chirality, similar to the skyrmions. With a further increase in h_z, the SkX phase melts into the SkG phase which is a gas of nucleated skyrmions, and finally transforms into a fully polarized FM phase. The SkG phase appears within a very narrow range of h_z at low temperatures and further work is needed to confirm its presence at those temperatures. But SkG is robust and primarily dominates at higher temperatures. For example, a typical spin configuration of the SkG phase, obtained at $h_z = 0.27$ and $T = 0.15$, is shown in Fig. 1(d).

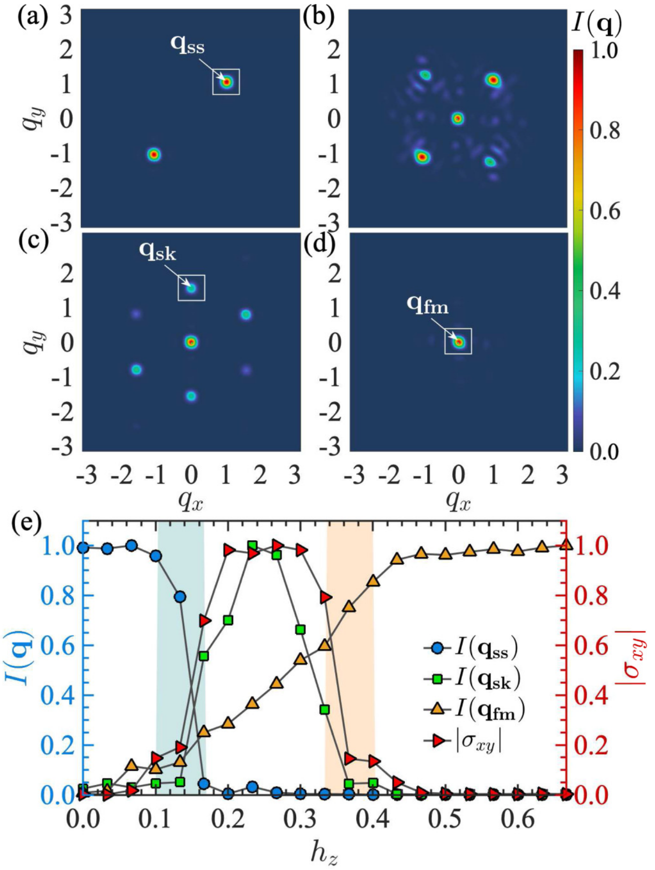

FIG. 3. Monte Carlo averaged intensity profile of the Bragg intensity $I(\mathbf{q})$ for magnetic field values (a) $h_z = 0$, (b) $h_z = 0.2$, (c) $h_z = 0.27$, and (d) $h_z = 0.37$, respectively. (e) Variation of the normalized $I(\mathbf{q})$ (left y axis) and Hall conductance σ_{xy} (right y axis) with h_z, at different characteristic momenta $\mathbf{q} = \mathbf{q}_{\mathrm{ss}}$, $\mathbf{q} = \mathbf{q}_{\mathrm{sk}}$, $\mathbf{q} = \mathbf{q}_{\mathrm{fm}}$, as indicated, respectively, in panels (a), (c), and (d). Panel (b) corresponds to the narrow bimeron regime, typically containing segments of "stripes" [panel (a)] involving both diagonals in the same configuration. The blue and yellow h_z regions in (e) show the field ranges where phase transitions occurs, likely first order in nature at $T = 0$. In all panels, the DM interaction is $D = 0.1$, the hopping amplitude $t_0 = 1$, the anisotropy strength $A = 0.05$, and the temperature $T = 0.001$.

The variation of the skyrmion number N_{sk} with h_z is depicted in Fig. 1(e) for three different values of D, revealing a clear enhancement within a range of h_z. At $T = 0$, N_{sk} should exhibit sharp first-order transitions at two critical values of h_z, clearly distinguishing the SkX phase from others. But here due to thermal fluctuations, the expected sharp first-order jumps are replaced by smooth crossovers as in Fig. 1(e). Increasing D, the h_z range where the SkX phase appears is enhanced. This is an anticipated behavior since a stronger DM interaction helps to stabilize the SkX phase.

In Figs. 3(a) to 3(d), we plot the MC-averaged Bragg intensity profile for the four different phases discussed in Fig. 1, *viz.* the SS, BM + Sk, SkX, and SkG. The SS and the SkX phases show, respectively, the single-**q** [Fig. 3(a)] and triple-**q** [Fig. 3(c)] structures of the spin configuration. Figure 3(b), for the BM + Sk phase, interestingly, displays a double-**q** spin configuration which is absent at $T = 0$. A similar double-**q** peak structure identified in neutron scattering measurement of $\mathrm{Co_8Zn_8Mn_4}$ was believed to originate in the formation of a square lattice of skyrmions [47]. Because of the large FM fraction, the SkG phase is dominated by the Bragg intensity at $\mathbf{q} = \mathbf{0}$ but with nonzero intensities at $\mathbf{q} \neq \mathbf{0}$ due to the randomly distributed skyrmions. Thus, $I(\mathbf{q_{fm}})$ in the SkG phase is not fully developed while $I(\mathbf{q_{sk}})$ is suppressed. The Bragg intensity $I(\mathbf{q})$ at different characteristic momenta, reveal a sequence of phase transitions, as shown in Fig. 3(e) where the transverse Hall conductance σ_{xy} is also plotted. Evidently, σ_{xy} [and also N_{sk} in Fig. 1(e)] become enhanced within a broader range of h_z than $I(\mathbf{q_{sk}})$, where $\mathbf{q} = \mathbf{q_{sk}}$ is the characteristic momentum for the SkX phase [as defined in Fig. 3(c)]. Note that the SS phase at low magnetic fields often involves a mixture of two mutually orthogonal spirals leading to labyrinth-like domains. In this context a small topological Hall conductance is induced due to the finite scalar spin chirality at the junctions of these orthogonal spirals. The SS and SkX phases can, therefore, be identified using $I(\mathbf{q_{ss}})$ and $I(\mathbf{q_{sk}})$, respectively, whereas, σ_{xy} and N_{sk} are suitable to identify the BM + Sk and the SkG phases. Antiferromagnetic skyrmion crystals are also reported to appear within a range of external magnetic fields in antiferromagnets with DM interactions [48].

IV. TEMPERATURE EVOLUTION

Having identified the phases appearing at various values of the external magnetic field at low temperatures, we explore the finite-temperature behavior of these phases. In Fig. 4(a), we show the temperature variation of the Bragg intensities $I(\mathbf{q_{fm}})$ and $I(\mathbf{q_{ss}})$ for the FM and SS phases in the absence of external magnetic fields at $D = 0$ and $D = 0.1$, respectively. The critical temperature $T_c^{\mathrm{SS}} \simeq 0.18$ for the SS phase appears to be rather close to that of the FM phase ($T_c^{\mathrm{FM}} \simeq 0.2$) which exists at the two-dimensional interface in the absence of DM interaction and external magnetic fields. For the phases associated with the skyrmions, we plot the Bragg intensity $I(\mathbf{q_{sk}})$, Hall conductance σ_{xy}, and skyrmion number N_{sk} versus T in Fig. 4(b) at a field $h_z = 0.27$. Evidently, $I(\mathbf{q_{sk}})$ drops faster with T than the other two observables, indicating that the SkX phase [here determined by an 80% drop in $I(\mathbf{q_{sk}})$, but other conventions lead to similar conclusions] exists at much lower temperatures than the SkG phase (determined by an 80% drop in N_{sk}). The critical temperatures for the SkX and the SkG phases at $h_z = 0.27$ are roughly $T_c^{\mathrm{SkX}} \simeq 0.09$ and $T_c^{SkG} \simeq 0.19$, respectively. The TH effect, although strongest at the SkX phase, exists at temperatures much above the SkX phase. There could be other contributions to the TH effect, and one potential origin is the skew scattering induced by the scalar spin chirality [8]. The skew-scattering induced TH effect appears near the transition to the SkX phase and is reflected by a change in the sign of the Hall conductance. In addition to the SkG phase, the BM + Sk phase also yields a finite contribution to the TH effect, as we shall discuss below.

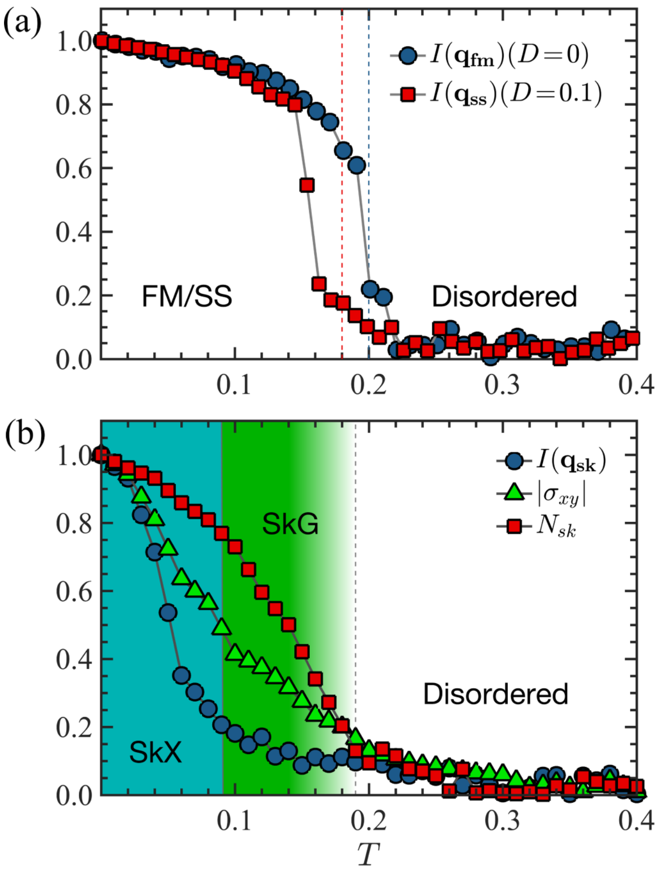

FIG. 4. (a) Monte Carlo results showing the temperature variation of the intensity $I(\mathbf{q_{fm}})$ for the FM phase (with zero DM interaction strength $D = 0$, nonzero anisotropy constant $A = 0.05$, and zero magnetic field $h_z = 0$) and intensity $I(\mathbf{q_{ss}})$ for the spin-spiral (SS) phase (at $D = 0.1$ and $h_z = 0$). The blue and red dashed lines provide a rough estimation of the critical temperatures here crudely defined as the temperatures where $I(\mathbf{q_{fm}})$ and $I(\mathbf{q_{ss}})$ drop to 20% of the $T = 0.001$ value. Panel (b) also shows Monte Carlo results for the intensity $I(\mathbf{q_{sk}})$ in the SkX regime, Hall conductance $|\sigma_{xy}|$, and skyrmion number N_{sk} (at $D = 0.1$ and $h_z = 0.27$). The critical temperature where $I(\mathbf{q_{sk}})$ drops to 20% of the value at $T = 0.001$ roughly defines the phase boundary of the skyrmion crystal (SkX) phase. Similarly, N_{sk} defines the phase boundary of the skyrmion gas (SkG) phase. All quantities in panels (a) and (b) are normalized to the respective values at the lowest temperature $T = 0.001$. Other parameters (t_0 and A) are the same as in Fig. 1. Using other reasonable cutoffs criteria to define critical temperatures leads to similar phase diagrams.

We constructed the phase diagrams for the manganite-iridate single interface in the temperature versus magnetic field plane. Results are depicted in Fig. 5 for three different values of the DM strength D. The phase diagrams show five different phases already discussed before *viz.* SS, SkX, BM + Sk, SkG, and FM. Note the BM + Sk and SkG regions are suppressed at very low temperatures. The FM phase, identified by both the Bragg intensity $I(\mathbf{q_{fm}})$ and the average out-of-plane magnetization M_z, does not have any phase boundary in the h_z-T plane and prevails in the high-field regime. The BM + Sk phase is identified by the overlap of the SS and the SkG phases, obtained, respectively, by $I(\mathbf{q_{ss}})$ and N_{sk}.

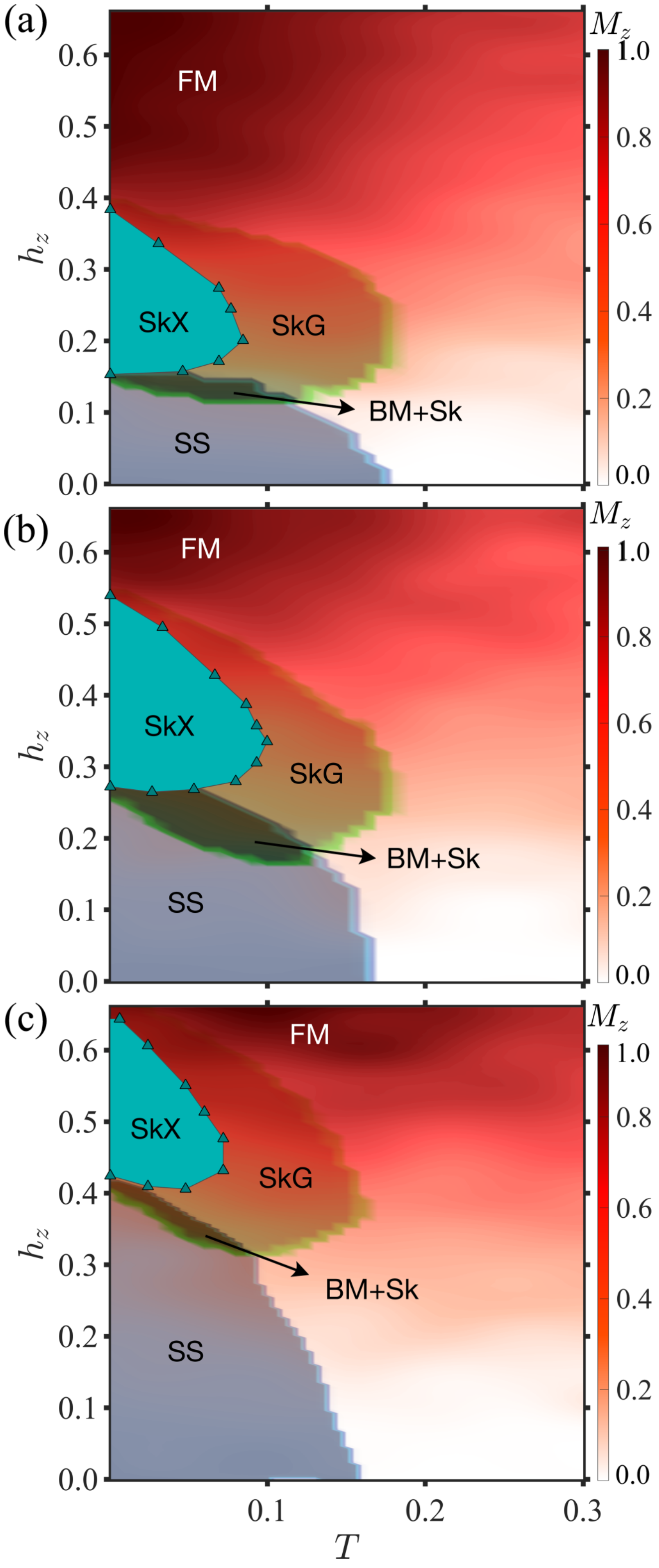

FIG. 5. Temperature (T) vs. magnetic field (h_z) phase diagrams for three different values of the DM interaction (a) $D = 0.1$, (b) $D = 0.15$, and (c) $D = 0.2$. The color bar represents the normalized average magnetization, perpendicular to the interface plane. The hopping amplitude is fixed to $t_0 = 1$ and the easy-plane anisotropy strength to $A = 0.05$.

Increasing D, the SS phase expands towards larger fields, which is expected since the DM interaction helps in stabilizing this SS phase. However, the critical temperature $T_c^{\rm SS}$ tends to decrease at very large D [noticeable in Fig. 5(c) for $D = 0.2$]. Very large values of D results in a SS phase with a spiral of short wavelength which makes the SS phase less susceptible to thermal fluctuations, accounting for the slow decrease in $T_c^{\rm SS}$ with increasing D. The SkX phase also moves towards higher fields with increasing D and is the largest in size (among the three plots shown in Fig. 5) for $D = 0.15$. For very large D, the skyrmion sizes are much smaller, comparable to the square lattice spacing, and, thus, the resulting SkX phase is vulnerable to thermal fluctuations. The results suggest that both the SS and the SkX phases are strongest at an optimal value of the DM interaction strength.

The results presented thus far are for a fixed value of the easy-plane anisotropy parameter $A = 0.05$. We have verified that a low-to-moderate value of the easy-plane anisotropy stabilizes the SkX phase, as found in a previous study [31]. Easy-axis anisotropy, on the other hand, suppresses the SkX phase, contrary to the cases of chiral and frustrated magnets [49,50].

V. $T = 0$ PHASE DIAGRAM

In the MC analysis discussed above, the lowest temperature accessed was $T = 0.001$. Below this temperature the MC procedure is less accurate because it is difficult to evolve away from nearly frozen metastable states. To complement the MC analysis with zero temperature results, we performed calculations of total energies of the three phases SS, SkX, and FM, by considering ideal spin configurations. We consider a 20×20 lattice with open boundary conditions, the same as in the above MC analysis, to compute the total energies of the three phases using the Hamiltonian Eq. (1), after optimizing the period of the spiral in the SS phase and the skyrmion radius and skyrmion-skyrmion separation in the SkX phase.

The variation of the total energies $E_{\rm SS}$, $E_{\rm SkX}$, and $E_{\rm FM}$ for the SS, SkX, and the FM phases, respectively, with respect to h_z at fixed DM interaction $D = 0.1$ is shown in Fig. 6, for two different values of the anisotropy parameter $A = 0.05$ and $A = 0.1$. By the minimum energy criterion, we can identify the most favorable spin configurations. For $A = 0.05$, we find that in the low-field regime $h_z \lesssim 0.23$, the SS phase has the lowest energy, while for $h_z \gtrsim 0.4$, the FM phase has the lowest energy. Remarkably, the SkX phase wins within an intermediate field range $0.23 < h_z < 0.4$, which is close to the field range predicted by the MC simulations. The transitions from the SS phase to the SkX phase and that from the SkX phase to the FM phase are first order at $T = 0$ (level crossing). With $A = 0.1$, we clearly observe that the SkX phase becomes wider with regards to the field range. It is interesting to note that $E_{\rm SS}$ is quite insensitive to the change in h_z in the SS phase and changes slope towards the second critical field value near the boundary between the SkX and the FM phases. $E_{\rm SkX}$ also changes its slope at the transition to the FM phase because of the drastic enhancement of the optimal radius of

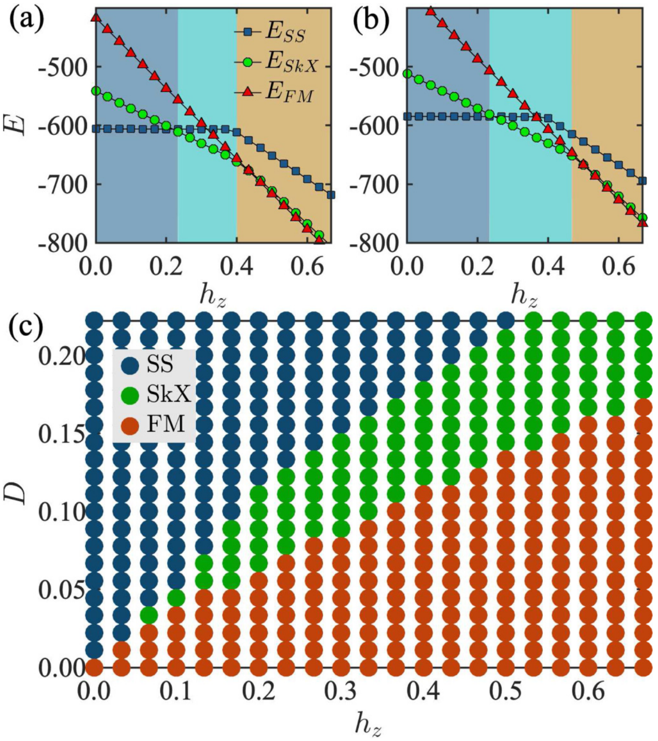

FIG. 6. Total energy of the ideal spin-spiral (SS), skyrmion-crystal (SkX), and ferromagnetic (FM) phases at zero temperature ($T = 0$) vs. the strength of the magnetic field h_z, at a fixed DM interaction strength $D = 0.1$. Panel (a) is at easy-plane anisotropy strength $A = 0.05$ and (b) at $A = 0.1$. These two panels show that the minimum-energy condition is satisfied for the SkX phase within a range of h_z values, in agreement with MC results. (c) Zero-temperature phase diagram in the h_z-D plane for $A = 0.05$ and $t_0 = 1$.

the skyrmions beyond a critical h_z, as noted before [31]. We tune D and plot the $T = 0$ phase diagram in Fig. 6(c) which reveals that, in general, the SkX phase becomes stronger with higher DM interaction and higher magnetic field.

VI. DISCUSSION AND CONCLUSION

The experimental critical temperature for the FM phase of a manganite-iridate interface appears within a range $100\text{ K} \lesssim T_c^{\text{FM}} \lesssim 300$ K, depending upon the thickness of the manganite layer [3]. From the MC analysis, we find $T_c^{\text{FM}} \approx 0.2t_0$ (with anisotropy parameter $A = 0.05$), which gives our hopping energy scale $t_0(=T_c^{\text{FM}}/0.2)$ as $40\text{ meV} \lesssim t_0 \lesssim 130$ meV. For a purely classical spin model with Heisenberg exchange term $-J\sum_{\langle ij\rangle}\mathbf{S}_i \cdot \mathbf{S}_j$, instead of the double-exchange term, we obtain $T_c^{\text{FM}} \simeq 7.5J$ with an anisotropy parameter $A = 0.05J$ (results gathered using a 20×20 cluster and MC simulations, not shown). By comparing the critical temperatures for the FM phase, obtained separately from the double-exchange model and classical spin model, we find the effective Heisenberg-exchange parameter for the considered double-exchange model to be $J \approx 0.03t_0$. The easy-plane anisotropy for LSMO films has been found to be $AS^2 \approx 0.21$ meV [51] which gives $A \approx 0.09$ meV with $S = 3/2$. Therefore, the critical DM interaction strength to realize the skyrmion crystal $D_c \sim \sqrt{JA}$ [52–54] appears in a range $0.3\text{ meV} \lesssim D_c \lesssim 0.6$ meV. LSMO also has a weak antiferromagnetic coupling [35] which has not been included in our description. Such a competing antiferromagnetic coupling will reduce the MC-estimated T_c^{FM} and, in turn, enhance D_c.

We realized skyrmions of radius approximately three unit cells with $D = 0.1t_0$. Increasing D will reduce the size of the skyrmions and when D is comparable to the hopping energy scale t_0, the skyrmion size be too small to be studied on a lattice. Conversely, very small values of D make the skyrmion size very large compared to the lattice sizes accessible. We therefore considered intermediate values of D where the skyrmion size is optimal for studying the SkX phase in the finite lattice where the spin-fermion model can be studied numerically. For similar reasons, the critical magnetic fields from the MC analysis are unrealistically large. Thus the main purpose here is to provide the *qualitative* variations of the skyrmion phases with D because we anticipate similar behavior at smaller energy scales.

To summarize, we investigated the TH effect arising from the scalar spin chirality of an emergent skyrmion crystal using a spin-fermionic model for a manganite-iridate interface. Using Monte Carlo calculations, we realized a nearly-triangular crystal of Néel-type skyrmions, arising within a finite range of external magnetic fields. A gas phase of well-formed independent skyrmions was also observed primarily at higher temperatures above the skyrmion crystal phase. Also, a mixed bimeron + skyrmion phase appears at finite temperatures between the spin-spiral phase and the skyrmion crystal phase. Topological Hall measurements, together with neutron-scattering experiments, can detect these complex phases.

We conclude that manganite-iridate interfaces offer a unique platform to explore unconventional magnetic and transport properties. We focused on the doping range in which LSMO is in its FM phase. The proximity effect from other types of magnetic phases, such as the antiferromagnetic phase or CE states, along with the large DM interaction, can lead to interesting phenomena [38,55]. The easy-plane anisotropy, which stabilizes the skyrmion crystal phase, can be modified using epitaxial strain, providing a useful knob to tune the TH effect. The DM interaction can be controlled by changing the thickness of the iridate layer, while the manganite layer thickness governs the level of spin polarization at the interface, opening a novel path towards efficient control of the TH effect by engineering multilayer heterostructures.

Note added. After finalizing our manuscript, we became aware of a recent experimental work on LSMO-SIO heterostructures [56]. They observed the enhancement of the Hall conductance at low magnetic fields and interpreted this behavior as the TH effect. Their results and interpretation are qualitatively consistent with our theoretical results.

ACKNOWLEDGMENTS

The authors gratefully acknowledge John Nichols, Elizabeth M. Skoropata, and Ho Nyung Lee for discussions on their related experiments. All members of this collaboration were supported by the US Department of Energy (DOE), Office of Science, Basic Energy Sciences (BES), Materials Sciences and Engineering Division. This research used resources of the Compute and Data Environment for Science (CADES) at the Oak Ridge National Laboratory, which is supported by the Office of Science of the US Department of Energy. This research was supported in part by an appointment to the Oak Ridge National Laboratory ASTRO Program, sponsored by the U.S. Department of Energy and administered by the Oak Ridge Institute for Science and Education.

[1] N. Nagaosa, J. Sinova, S. Onoda, A. H. MacDonald, and N. P. Ong, Anomalous Hall effect, Rev. Mod. Phys. **82**, 1539 (2010).

[2] S. Onoda, N. Sugimoto, and N. Nagaosa, Intrinsic Versus Extrinsic Anomalous Hall Effect in Ferromagnets, Phys. Rev. Lett. **97**, 126602 (2006).

[3] J. Nichols, X. Gao, S. Lee, T. L. Meyer, J. W. Freeland, V. Lauter, D. Yi, J. Liu, D. Haskel, J. R. Petrie, E.-J. Guo, A. Herklotz, D. Lee, T. Z. Ward, G. Eres, M. R. Fitzsimmons, and H. N. Lee, Emerging magnetism and anomalous Hall effect in iridate-manganite heterostructures, Nat. Commun. **7**, 12721 (2016).

[4] M. Diez, A. M. R. V. L. Monteiro, G. Mattoni, E. Cobanera, T. Hyart, E. Mulazimoglu, N. Bovenzi, C. W. J. Beenakker, and A. D. Caviglia, Giant Negative Magnetoresistance Driven by Spin-Orbit Coupling at the $LaAlO_3/SrTiO_3$ Interface, Phys. Rev. Lett. **115**, 016803 (2015).

[5] M. Onoda, G. Tatara, and N. Nagaosa, Anomalous Hall effect and skyrmion number in real and momentum spaces, J. Phys. Soc. Jpn. **73**, 2624 (2004).

[6] S. D. Yi, S. Onoda, N. Nagaosa, and J. H. Han, Skyrmions and anomalous Hall effect in a Dzyaloshinskii-Moriya spiral magnet, Phys. Rev. B **80**, 054416 (2009).

[7] K. Hamamoto, M. Ezawa, and N. Nagaosa, Quantized topological Hall effect in skyrmion crystal, Phys. Rev. B **92**, 115417 (2015).

[8] H. Ishizuka and N. Nagaosa, Spin chirality induced skew scattering and anomalous Hall effect in chiral magnets, Sci. Adv. **4**, eaap9962 (2018).

[9] J. Matsuno, N. Ogawa, K. Yasuda, F. Kagawa, W. Koshibae, N. Nagaosa, Y. Tokura, and M. Kawasaki, Interface-driven topological Hall effect in $SrRuO_3$-$SrIrO_3$ bilayer, Sci. Adv. **2**, e1600304 (2016).

[10] L. Wang, Q. Feng, Y. Kim, R. Kim, K. H. Lee, S. D. Pollard, Y. J. Shin, H. Zhou, W. Peng, D. Lee, W. Meng, H. Yang, J. H. Han, M. Kim, Q. Lu, and T. W. Noh, Ferroelectrically tunable magnetic skyrmions in ultrathin oxide heterostructures, Nat. Mater. **17**, 1087 (2018).

[11] M. Nakamura, D. Morikawa, X. Yu, F. Kagawa, T. Arima, Y. Tokura, and M. Kawasaki, Emergence of topological Hall effect in half-metallic manganite thin films by tuning perpendicular magnetic anisotropy, J. Phys. Soc. Jpn. **87**, 074704 (2018).

[12] L. Vistoli, W. Wang, A. Sander, Q. Zhu, B. Casals, R. Cichelero, A. Barthélémy, S. Fusil, G. Herranz, S. Valencia, R. Abrudan, E. Weschke, K. Nakazawa, H. Kohno, J. Santamaria, W. Wu, V. Garcia, and M. Bibes, Giant topological Hall effect in correlated oxide thin films, Nat. Phys. **15**, 67 (2019).

[13] A. Neubauer, C. Pfleiderer, B. Binz, A. Rosch, R. Ritz, P. G. Niklowitz, and P. Böni, Topological Hall Effect in the A Phase of MnSi, Phys. Rev. Lett. **102**, 186602 (2009).

[14] N. Kanazawa, Y. Onose, T. Arima, D. Okuyama, K. Ohoyama, S. Wakimoto, K. Kakurai, S. Ishiwata, and Y. Tokura, Large Topological Hall Effect in a Short-Period Helimagnet MnGe, Phys. Rev. Lett. **106**, 156603 (2011).

[15] Y. Taguchi, Y. Oohara, H. Yoshizawa, N. Nagaosa, and Y. Tokura, Spin chirality, Berry phase, and anomalous Hall effect in a frustrated ferromagnet, Science **291**, 2573 (2001).

[16] K. G. Rana, O. Meshcheriakova, J. Kübler, B. Ernst, J. Karel, R. Hillebrand, E. Pippel, P. Werner, A. K. Nayak, C. Felser, and S. S. P. Parkin, Observation of topological Hall effect in Mn_2RhSn films, New J. Phys. **18**, 085007 (2016).

[17] P. Swekis, A. Markou, D. Kriegner, J. Gayles, R. Schlitz, W. Schnelle, S. T. B. Goennenwein, and C. Felser, Topological Hall effect in thin films of $Mn_{1.5}PtSn$, Phys. Rev. Mater. **3**, 013001 (2019).

[18] P. Vir, J. Gayles, A. S. Sukhanov, N. Kumar, F. Damay, Yan Sun, J. Kübler, C. Shekhar, and C. Felser, Anisotropic topological Hall effect with real and momentum space Berry curvature in the antiskrymion-hosting Heusler compound $Mn_{1.4}PtSn$, Phys. Rev. B **99**, 140406 (2019).

[19] S. Banerjee, O. Erten, and M. Randeria, Ferromagnetic exchange, spin-orbit coupling and spiral magnetism at the $LaAlO_3/SrTiO_3$ interface, Nat. Phys. **9**, 626 (2013).

[20] X. Li, W. V. Liu, and L. Balents, Spirals and Skyrmions in Two Dimensional Oxide Heterostructures, Phys. Rev. Lett. **112**, 067202 (2014).

[21] S. Mühlbauer, B. Binz, F. Jonietz, C. Pfleiderer, A. Rosch, A. Neubauer, R. Georgii, and P. Böni, Skyrmion lattice in a chiral magnet, Science **323**, 915 (2009).

[22] M. Ezawa, Compact merons and skyrmions in thin chiral magnetic films, Phys. Rev. B **83**, 100408 (2011).

[23] S. X. Huang and C. L. Chien, Extended Skyrmion Phase in Epitaxial FeGe(111) Thin Films, Phys. Rev. Lett. **108**, 267201 (2012).

[24] X. Z. Yu, Y. Tokunaga, Y. Kaneko, W. Z. Zhang, K. Kimoto, Y. Matsui, Y. Taguchi, and Y. Tokura, Biskyrmion states and their current-driven motion in a layered manganite, Nat. Commun. **5**, 3198 (2014).

[25] A. Bogdanov and A. Hubert, Thermodynamically stable magnetic vortex states in magnetic crystals, J. Magn. Magn. Mater. **138**, 255 (1994).

[26] R. Ozawa, S. Hayami, and Y. Motome, Zero-Field Skyrmions with a High Topological Number in Itinerant Magnets, Phys. Rev. Lett. **118**, 147205 (2017).

[27] S. Hayami and Y. Motome, Effect of magnetic anisotropy on skyrmions with a high topological number in itinerant magnets, Phys. Rev. B **99**, 094420 (2019).

[28] J. G. Zhao, L. X. Yang, Y. Yu, F. Y. Li, R. C. Yu, Z. Fang, L. C. Chen, and C. Q. Jin, High-pressure synthesis of orthorhombic $SrIrO_3$ perovskite and its positive magnetoresistance, J. Appl. Phys. **103**, 103706 (2008).

[29] H. Jalili, Y. Chen, and B. Yildiz, Structural, chemical, and electronic state on $La_{0.7}Sr_{0.3}MnO_3$ dense thin-film surfaces at high temperature: Surface segregation, ECS Trans. **28**, 235 (2010).

[30] S. Okamoto, J. Nichols, C. Sohn, S. Y. Kim, T. W. Noh, and H. N. Lee, Charge transfer in iridate-manganite superlattices, Nano Lett. **17**, 2126 (2017).

[31] S. Banerjee, J. Rowland, O. Erten, and M. Randeria, Enhanced Stability of Skyrmions in Two-Dimensional Chiral Magnets with Rashba Spin-Orbit Coupling, Phys. Rev. X **4**, 031045 (2014).

[32] S. Dong, H. Xiang, and E. Dagotto, Magnetoelectricity in multiferroics: a theoretical perspective, arXiv:1902.01532 [Natl. Sci. Rev. (to be published)].

[33] S. Buhrandt and L. Fritz, Skyrmion lattice phase in three-dimensional chiral magnets from Monte Carlo simulations, Phys. Rev. B **88**, 195137 (2013).

[34] M. N. Wilson, A. B. Butenko, A. N. Bogdanov, and T. L. Monchesky, Chiral skyrmions in cubic helimagnet films: The role of uniaxial anisotropy, Phys. Rev. B **89**, 094411 (2014).

[35] E. Dagotto, T. Hotta, and A. Moreo, Colossal magnetoresistant materials: the key role of phase separation, Phys. Rep. **344**, 1 (2001).

[36] A. Moreo, M. Mayr, A. Feiguin, S. Yunoki, and E. Dagotto, Giant Cluster Coexistence in Doped Manganites and Other Compounds, Phys. Rev. Lett. **84**, 5568 (2000).

[37] S. Yunoki, T. Hotta, and E. Dagotto, Ferromagnetic, A-type, and Charge-Ordered CE-Type States in Doped Manganites Using Jahn-Teller Phonons, Phys. Rev. Lett. **84**, 3714 (2000).

[38] T. Hotta, M. Moraghebi, A. Feiguin, A. Moreo, S. Yunoki, and E. Dagotto, Unveiling New Magnetic Phases of Undoped and Doped Manganites, Phys. Rev. Lett. **90**, 247203 (2003).

[39] S. Kumar and P. Majumdar, A traveling cluster approximation for lattice fermions strongly coupled to classical degrees of freedom, Eur. Phys. J. B **50**, 571 (2006).

[40] A. Mukherjee, N. D. Patel, C. Bishop, and E. Dagotto, Parallelized traveling cluster approximation to study numerically spin-fermion models on large lattices, Phys. Rev. E **91**, 063303 (2015).

[41] I. A. Iakovlev, O. M. Sotnikov, and V. V. Mazurenko, Bimeron nanoconfined design, Phys. Rev. B **97**, 184415 (2018).

[42] E. Müller-Hartmann and E. Dagotto, Electronic Hamiltonian for transition-metal oxide compounds, Phys. Rev. B **54**, R6819 (1996).

[43] S. Heinze, K. von Bergmann, M. Menzel, J. Brede, A. Kubetzka, R. Wiesendanger, G. Bihlmayer, and S. Blügel, Spontaneous atomic-scale magnetic skyrmion lattice in two dimensions, Nat. Phys. **7**, 713 (2011).

[44] N. Nagaosa and Y. Tokura, Topological properties and dynamics of magnetic skyrmions, Nat. Nanotechnol. **8**, 899 (2013).

[45] H. Ding and C. Shu, A stencil adaptive algorithm for finite difference solution of incompressible viscous flows, J. Comput. Phys. **214**, 397 (2006).

[46] R. L. Silva, L. D. Secchin, W. A. Moura-Melo, A. R. Pereira, and R. L. Stamps, Emergence of skyrmion lattices and bimerons in chiral magnetic thin films with nonmagnetic impurities, Phys. Rev. B **89**, 054434 (2014).

[47] K. Karube, J. S. White, N. Reynolds, J. L. Gavilano, H. Oike, A. Kikkawa, F. Kagawa, Y. Tokunaga, H. M. Rønnow, Y. Tokura, and Y. Taguchi, Robust metastable skyrmions and their triangular-square lattice structural transition in a high-temperature chiral magnet, Nat. Mater. **15**, 1237 (2016).

[48] S. A. Díaz, J. Klinovaja, and D. Loss, Topological Magnons and Edge States in Antiferromagnetic Skyrmion Crystals, Phys. Rev. Lett. **122**, 187203 (2019).

[49] A. B. Butenko, A. A. Leonov, U. K. Rößler, and A. N. Bogdanov, Stabilization of skyrmion textures by uniaxial distortions in noncentrosymmetric cubic helimagnets, Phys. Rev. B **82**, 052403 (2010).

[50] S. Hayami, S.-Z. Lin, and C. D. Batista, Bubble and skyrmion crystals in frustrated magnets with easy-axis anisotropy, Phys. Rev. B **93**, 184413 (2016).

[51] H. Boschker, M. Mathews, P. Brinks, E. Houwman, A. Vailionis, G. Koster, D. H.A. Blank, and G. Rijnders, Uniaxial contribution to the magnetic anisotropy of $La_{0.67}Sr_{0.33}MnO_3$ thin films induced by orthorhombic crystal structure, J. Magn. Magn. Mater. **323**, 2632 (2011).

[52] M. Hervé, B. Dupé, R. Lopes, M. Böttcher, M. D. Martins, T. Balashov, L. Gerhard, J. Sinova, and W. Wulfhekel, Stabilizing spin spirals and isolated skyrmions at low magnetic field exploiting vanishing magnetic anisotropy, Nat. Commun. **9**, 1015 (2018).

[53] U. K. Rößler, A. N. Bogdanov, and C. Pfleiderer, Spontaneous skyrmion ground states in magnetic metals, Nature **442**, 797 (2006).

[54] S. Rohart and A. Thiaville, Skyrmion confinement in ultrathin film nanostructures in the presence of Dzyaloshinskii-Moriya interaction, Phys. Rev. B **88**, 184422 (2013).

[55] S. Dong, K. Yamauchi, S. Yunoki, R. Yu, S. Liang, A. Moreo, J.-M. Liu, S. Picozzi, and E. Dagotto, Exchange Bias Driven by the Dzyaloshinskii-Moriya Interaction and Ferroelectric Polarization at G-Type Antiferromagnetic Perovskite Interfaces, Phys. Rev. Lett. **103**, 127201 (2009).

[56] Y. Li, L. Zhang, Q. Zhang, C. Li, T. Yang, Y. Deng, L. Gu, and D. Wu, Emergent topological Hall effect in $La_{0.7}Sr_{0.3}MnO_3/SrIrO_3$ heterostructures, ACS Appl. Mater. Interfaces **11**, 21268 (2019).